ADVANCED ENERGY MATERIALS
www.advenergymat.de

Rationalizing Performance Losses of Wide Bandgap Perovskite Solar Cells Evident in Data from the *Perovskite Database*

Klara Suchan, T. Jesper Jacobsson, Carolin Rehermann, Eva L. Unger,* Thomas Kirchartz, and Christian M. Wolff**

Metal halide perovskites (MHPs) have become a widely studied class of semiconductors for various optoelectronic devices. The possibility to tune their bandgap (E_g) over a broad spectral range from 1.2 eV to 3 eV by compositional engineering makes them particularly attractive for light emitting devices and multi-junction solar cells. In this metadata study, data from Peer-reviewed publications available in the *Perovskite Database* (www.perovskitedatabase.com) is used to evaluate the current state of E_g tuning in *wide* E_g MHP semiconductors. Recent literature on wide E_g MHP semiconductors is examined and the data is extracted and uploaded onto the *Perovskite Database*. Beyond describing recent highlights and scientific breakthroughs, general trends are drawn from 45,000 individual experimental datasets of MHP solar cell devices. The historical evolution of MHP solar cells is recapitulated, and general conclusions are drawn about the current limits of device performance. Three dominant causes are identified and discussed for the degradation of performance relative to the Shockley-Queisser (SQ) model's theoretical limit for single-junction solar cells: 1) energetically mismatched selective transport materials for wide Eg MHPs, 2) lower optoelectronic quality of wide E_g MHP absorbers, and 3) dynamically evolving compositional heterogeneity due to light-induced phase segregation phenomena.

1. Introduction

Semiconductor material families with an ideally continuously tunable bandgap (E_g) are at the heart of the technology of optoelectronic devices of the 21st century. While the family of III-V semiconductors is a well-established class of vacuum-processed materials that are currently dominating the field of light-emitting devices and concentrator photovoltaics, metal-halide perovskites (MHPs) are a much newer and less-established class of semiconductors with tunable E_gs that can be processed from solution and have a significant potential for photovoltaics. E_g tuning is of high technological importance in solar cells, as it paves the way to effectively reduce the cost of energy conversion by achieving higher power conversion efficiencies in tandem or multi-junction solar cells. The particular challenge of multi-junction solar cells is the requirement to split the solar spectrum[1] into n equal parts,

K. Suchan, E. L. Unger
Division of Chemical Physics and NanoLund
Lund University
Box 124, 22100 Lund, Sweden
E-mail: klara.suchan@sljus.lu.se; eva.unger@helmholtz-berlin.de

T. J. Jacobsson, C. Rehermann, E. L. Unger
Helmholtz-Zentrum Berlin für Materialien und Energie GmbH
HySPRINT Innovation Lab: Hybrid Materials Formation and Scaling
Kekuléstraße 5, 12489 Berlin, Germany

The ORCID identification number(s) for the author(s) of this article can be found under https://doi.org/10.1002/aenm.202303420

DOI: 10.1002/aenm.202303420

T. J. Jacobsson
Institute of Photoelectronic Thin Film Devices and Technology
Key Laboratory of Photoelectronic Thin Film Devices and Technology of Tianjin
College of Electronic Information and Optical Engineering
Nankai University
Nankai, Tianjin 300350, China

T. Kirchartz
IEK5-Photovoltaics
Forschungszentrum Jülich
52425 Jülich, Germany

T. Kirchartz
Faculty of Engineering and CENIDE
University of Duisburg-Essen
Carl-Benz-Straße 199, 47057 Duisburg, Germany

C. M. Wolff
STI IEM PV-LAB
Ecole Polytechnique Fédérale de Lausanne (EPFL)
Rue de la Maladière 71b, Neuchâtel 2000, Switzerland
E-mail: chriwolff@uni-potsdam.de

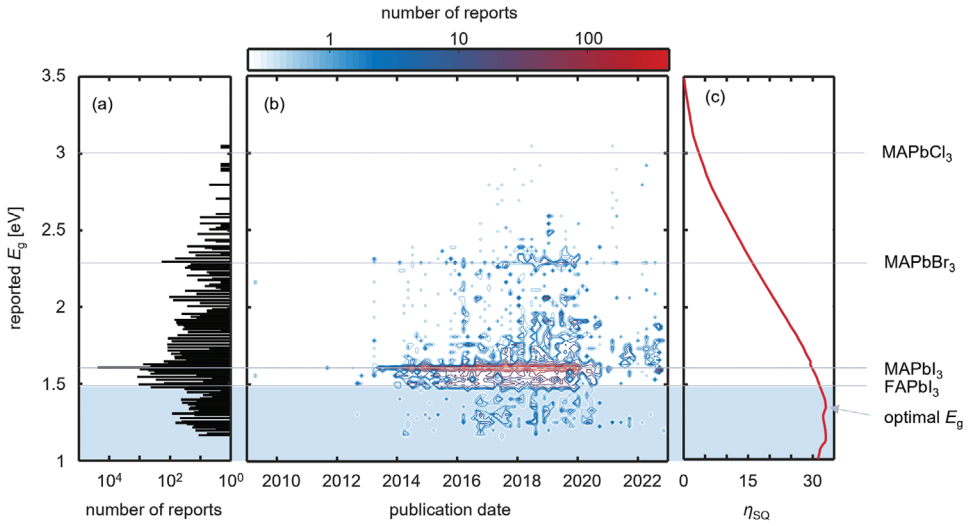

Figure 1. a) Histogram of perovskite E_g distribution. The bin size is 0.02 eV. b) Evolution of the reported E_g in the literature. 1.6 eV perovskites dominate the reports throughout the years, and even in the 2022s, most research is conducted on formulations close to pure $MAPbI_3$ (1.6 eV) and $FAPbI_3$ (1.5 eV). c) Comparison with the PCE in the SQ-limit shows that the most exploited E_g region is above the optimal E_g region for single-junction solar cells.

where n is the number of junctions. For double-junction solar cells, the ideal E_gs of the bottom and top absorbers have been determined to be about 0.9 eV and 1.6 eV, respectively.[2] For triple-junction solar cells, the E_gs of the bottom, middle, and top cells should ideally be 0.7 eV, 1.2 eV, and 1.8 eV, respectively.[2] Assuming the bottom cell is fixed and based on crystalline silicon (c-Si), the optimal E_g of the top cell of a double-junction solar cell is around 1.7–1.75 eV,[3–5] and 1.4–1.5 eV and 1.9–2.1 eV, respectively, for a triple-junction.[4] Complete absorption above the E_g with an instantaneous onset is a good first-order approximation, yet real materials have non-instantaneous absorption onsets, raising the question of what the E_g for a real material is. This is discussed in greater detail in the Supporting Information (S1), but regardless of the precise definition, adjusting the E_gs and thicknesses of the different semiconductors is the most direct way to ensure that the solar spectrum is split to minimize losses in a multi-junction solar cell. Over the last few years, experimental implementations of tandem cells based on MHP/silicon combinations have shown rapid improvements,[6,7] reaching over 33%,[8] now exceeding the Shockley-Queisser limit (SQ-limit)[9,10] of single-junction solar cells[]. Further interest lies in the architectural domain, where solar cells with different colour appearances are in demand for building-integrated photovoltaics (BIPV). Moreover, their E_g tuning also allows the realization of photodetectors or light-emitting diodes[11–13] with a wide range of detection ranges or emission wavelengths.

While crystaline silicon (c-Si), the workhorse of modern electronics, has a room temperature E_g of 1.12 eV, III-V semiconductors based on gallium, indium, phosphorus, antimony, and arsenide are tunable over a wide E_g range from 0.2 to 2.7 eV. This E_g tunability has enabled modern light-emitting and laser diodes[14] and high-efficiency multi-junction solar cells with applications in concentrator solar cells and onboard satellites.[15] However, the high production cost of high-quality III-V materials has limited the applications to products where a sufficiently high economic benefit can compensate for the high cost per area. Thus, a class of materials that combines E_g tunability, high material quality, and low-cost processing is of great interest for optoelectronics and photovoltaics. The discovery of MHPs, which exhibit optoelectronic properties comparable to those of III-V materials while being processed at low temperatures from earth-abundant materials, has led to intense research activities and several technological breakthroughs for applications in solar cells and light-emitting devices.[16–19] The E_g of MHP semiconductors can be tuned by a (partial) substitution of the constituent ions on all three sites of the generic ABX_3 perovskite structure.[20] While methylammonium lead triiodide ($MAPbI_3$) was the archetypal MHP compound, a wider range of constituents has been discovered for all three crystal sites. The most commonly used ions on the A site are cesium (Cs^+), methylammonium (MA^+), and formamidinium (FA^+); at the B site, lead (Pb^{2+}) and tin (Sn^{2+}); and at the X site, iodide (I^-), bromide (Br^-), or chloride (Cl^-). This enabled spanning a E_g range from 1.2 eV for $MAPb_{0.5}Sn_{0.5}I_3$,[21] to >3 eV for $MAPbCl_3$,[22] as shown in **Figure 1**. The ability to modify the E_g within a technologically relevant range for one family of materials is a necessary but not sufficient condition to enable a wide range of applications. Maintaining high material quality, compositional homogeneity and stability, and good electrical properties over a wide E_g range are critical requirements for efficient device performance. Other material families, such as $Cu(In,Ga)(Se,S)_2$, have not yet been able to achieve high power conversion efficiencies (PCEs) over a wide E_g range, limiting their use in tandem applications.[23–25]

Herein, we evaluate the current status and recent progress in the E_g tuning and photovoltaic performance of metal halide perovskites over the entire E_g range from 1.2 to 3 eV, with a particular focus on wide E_g materials with $E_g > 1.6$ eV. While a material's "quality" is partly determined by its intended use, it is generally essential to have low non-radiative losses in the absorbing material, low resistive and recombination losses at the interfaces and within the transport materials, high stability and reliability. Therefore, the following discussion is of general relevance

to other applications as well, since the photovoltaic PCE achieved reflects the intrinsic optoelectronic quality of the absorber and the energetic losses introduced by the transport materials.

This metadata study provides an overview of the E_g regions where photovoltaic performance is still suboptimal. While MHP devices with a E_g of around 1.6 eV show astonishing performance, the performance in other E_g regions still needs further efforts to reach a similar level. In particular, there is room for improvement below 1.4 eV, the E_g region theoretically optimal for single-junction photovoltaics, and above 1.6 eV, the range optimal for the top cell in multi-junction applications. We evaluate material defects, energetic mismatch of the transport materials, and chemical instability of the absorber as the mechanisms at the core of the performance degradation. We argue that a limited exploration of suitable selective transport materials currently limits the performance of MHP devices at all E_gs other than the archetypal 1.5-1.6 eV of $MAPbI_3$ and $FAPbI_3$, calling for more extensive testing and development of selective transport materials, especially for wide E_g devices. In addition, we highlight the inferior luminescence quantum efficiency of mixed iodide-bromide perovskites, likely related to the widely reported light-induced phase segregation. We aim to show which approaches have successfully overcome the performance limitations and thus help direct future research efforts.

Beyond this discussion of the current status of metal halide perovskite applications themselves, we present the opportunities that lie in databases such as *The Perovskite Database*,[26] which is accessible via www.perovskitedatabase.com. This database project collected a significant fraction of the accumulated historical data published in metal halide perovskite solar cell devices, with data from >45,000 individual solar cell devices. For 31,616 of these devices, the E_g of the perovskite absorber was either explicitly reported or inferred from reported absorption or EQE data during data extraction for *The Perovskite Database*.[26] The use of the database allows us to conclude general trends and shortcomings in perovskite research from a large body of knowledge rather than individual reports. In addition, we point out the limitations of the current database and analyse how future databases should be improved to allow more in-depth analyses by reporting more of the fundamental properties of the absorber materials. The dataset currently available in the database consists of single metric or numeric values detailing a variety of sample descriptors such as absorber composition and device layer stack in combination with solar cell device performance metrics. The initial dataset of *The Perovskite Database* entries was collected collaboratively by >80 participants to extract data from the published literature and uploaded in early 2021.[26] For this metadata study, we identified recent publications not yet in the database, with a particular focus on "wide" E_g perovskites as well as "E_g tuning", published between 2021 and 2023. Data from these publications have been extracted according to our standardised extraction protocol and uploaded to the database. Still, we would like to explicitly encourage colleagues to add their latest results to the database, ensuring a more complete and correct data collection.

2. Bandgap-Dependent Performance

The E_gs of MHPs used for solar cells stretch from 1.2 to over 3 eV (Figure 1a). However, the distribution of reported devices within this E_g range is far from uniform, with most entries around 1.55–1.65 eV. This E_g range includes $MAPbI_3$, which, since the initial reports in 2012, has been the most researched MHP (Figure 1b). Since 2014, perovskites with E_gs around 1.5 eV, which includes $FAPbI_3$, have increased. While 1.50–1.65 eV is slightly above the optimal E_g range for single-junction solar cells,[27] MHP semiconductors with wide E_gs > 1.6 eV are of interest as a complementary wide E_g absorber to existing photovoltaic technologies such as c-Si (E_g = 1.1eV) and GaAs (E_g = 1.4eV) in multi-junction solar cells.

Exploring lower E_g regions using MHPs requires the introduction of tin on the B-site of the perovskite crystal structure, as demonstrated in 2014. The discovery thereof enabled MHP formulations with E_gs below 1.4 eV, referred to as a narrow-E_g. This E_g range is suitable for single-junction cells and the bottom cell in a perovskite-perovskite tandem cell. Such narrow-E_g perovskites in the maximum of the SQ-limit, (Figure 1c) show thus potential as an alternative to the cost-intensive GaAs or even c-Si-based solar cells.

The prospect of multi-junction devices has sparked a broader interest in MHPs with wide E_gs since ≈ 2016. By substituting a small fraction of iodide with bromide, E_gs around 1.7 eV can be reached, which is ideal for a top absorber in a silicon-perovskite tandem device. By increasing the bromide content, E_gs above 1.8 eV can be reached. Still, reports in that E_g range are rare, probably due to a lack of applications in solar cells and challenges with chemical photo-stability. Mixed bromide-iodide perovskites are discussed further below.

What constitutes a *good* material is application-dependent, but for solar cells, high optoelectronic quality is often referred to in terms of high charge carrier mobility, long lifetimes, or high luminescence quantum efficiency. Given the close link between those properties and solar cell efficiency and the performance of almost any optoelectronic device, the vast amount of data on solar cell performance can be used as a proxy for the general optoelectronic quality of metal halide perovskites. MHPs may have a broadly tuneable E_g, but that does not necessarily mean that high-quality perovskites with any E_g can be produced. This becomes evident if the solar cell performance of all reported devices is analyzed as a function of the E_g.

Figure 2a shows the cell efficiency vs. the perovskite E_g, with colours indicating the publication year, alongside the theoretical maximum, that is, the SQ-limit.[27] Noticeable is again the pronounced data point density in the E_g range around 1.6 eV corresponding to $MAPbI_3$. From this simple representation, the great success of MHPs becomes evident, with top efficiencies reaching close to the theoretical limit in the E_g range of around 1.55–1.6 eV. It is worth noticing that this E_g range is significantly higher than the maxima of the SQ-limit at 1.33 eV and 1.1 eV, Figure 2a.[27] This hints at an untapped potential if a similar optoelectronic quality could also be reached for those narrow-E_g perovskites.

A more detailed view can be obtained by normalizing the performance metrics relative to the SQ-limit. This is done in Figure 2b–d, where the relative PCE (η/η_{SQ}), open circuit voltage ($V_{OC,\,SQ} - V_{OC}$) and short circuit current ($J_{SC}/J_{SC,\,SQ}$) from the perovskite database devices are plotted against the reported E_g, binned in 0.02 eV increments. For large E_g ranges, both the average and the maximum η/η_{SQ} are reasonably constant. Still, there are also regions where the performance is worse. Most

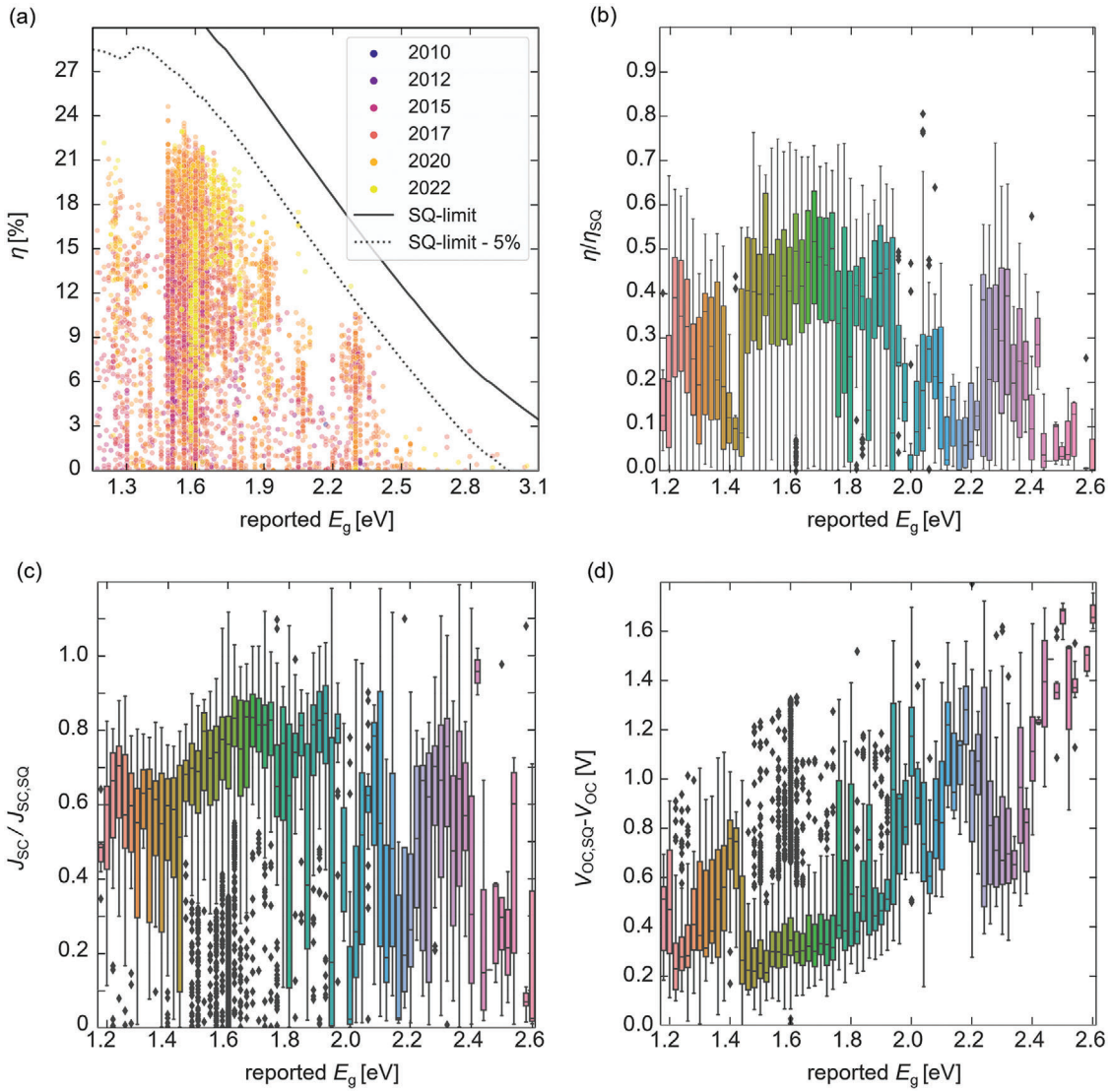

Figure 2. a) Device efficiency as a function of the reported perovskite E_g for all cells in *The Perovskite Database* together with the SQ-limit (solid) and the SQ-limit minus 5% (broken). The colour of the dot represents the publication date. Box plots of (b) the cell efficiency vs. perovskite E_g, (c) the short circuit current, J_{SC}, and (d) the V_{OC} loss, that is, $V_{OC,\,SQ} - V_{OC}$, as a function of the E_g. Both the PCE and J_{SC} are normalised with the values given by the SQ-limit, that is, η/η_{SQ} and $J_{SC}/J_{SC,\,SQ}$. The bin size is 0.02 eV, and the leftmost bin is at 1.18 eV. The end of the boxes represents the 25 and the 75 percentiles. The whiskers are placed at an interquartile range of 1.5, which means that for a normal distributed dataset, 99.3 % of points should be within that range.

notably around 1.45 eV, just below the E_g of $FAPbI_3$ and between 1.9 eV and 2.2 eV. Most of those performance dips are also reflected in the average $J_{SC}/J_{SC,\,SQ}$, which gradually rises with increased E_g until it plateaus around 1.6 eV, followed by dips between 1.8 eV and 2.2 eV. For E_gs around 2.3 eV, primarily corresponding to pure $MAPbBr_3$, the performance utilization again increases to values close to the top region around 1.6 eV. For perovskites with even wider E_gs, the performance is again poor, both in absolute and relative terms. The trend in the V_{OC} loss, that is, $V_{OC,\,SQ} - V_{OC}$, is somewhat different. The minimum, that is, the lowest average loss, happens for cells with a E_g around 1.5 eV, slightly below that for pure $MAPbI_3$. With increasing E_g, the V_{OC} loss does not stay constant but gradually increases with additional spikes in the regions around 1.8, 2.0, 2.15, and above 2.3 eV.

There are several possible E_g-dependent reasons behind the dips in the utilized theoretical performance seen in Figure 2. For narrow-E_g MHPs, there are fundamental challenges in the material stability, such as Sn^{2+} oxidation. Light-induced phase segregation has been discussed for wide E_g bromide-rich mixed MHPs to lead to open circuit voltage pinning.[28,29] Those challenges and strategies to overcome them will be discussed in detail in the following sections. The observations are also affected by effort. The best-performing devices, both in absolute and relative terms, are found in the E_g ranges with the most significant number of reported devices. This is consistent with recent reports on the universality of progress in solar cell research in general as a function of the accumulated number of publications as an assay of the accumulated research effort.[30] The rest of the device stack

has also primarily been optimized for perovskite formulations close to $MAPbI_3$, which may result in energy misalignments for narrow and wide E_g perovskites.

Another crucial performance metric is operational stability, a significant concern from the earliest reports. Stability is not as frequently reported as the standard *JV* metrics, and only 17% of the devices in the perovskite database have some form of stability measurement reported. Of those, only 3,000 devices have the initial and the final PCE disseminated. This includes tests ranging from short stability measurements in a dark and dry atmosphere under open-circuit conditions to extended measurements under maximum power point (MPP) tracking under hot and humid conditions. This results in less comparability between individual data points. However, it seems like the devices that perform best after a stability test tend to have a slightly wider E_g than the devices that performed best before any stability measurement, that is, slightly above 1.6 eV rather than under 1.6 eV.

3. Wide Bandgap Metal Halide Perovskites: Mixing Bromides and Iodides

A signature feature of $MAPbI_3$ perovskites has been their small V_{OC}-loss compared to the SQ-limit. For top performing $(MA,FA)PbI_3$ perovskites, it lies as low as 60 mV, slightly above values for GaAs solar cells.[31,7] Considering the database's reported devices, the smallest voltage losses can be found in the E_g region around 1.45 eV, with an average open circuit loss of slightly above 200 mV. Unfortunately, the V_{OC} loss can increase continuously with increasing E_g, as shown in Figure 2b. Additionally, there are spikes of voltage loss at specific E_g regions around 1.75 eV, 2.0 eV, and above 2.2 eV.

While the $J_{sc}$is increasing at first when the E_g increases, it shows correlated drops at the same E_g regions, and there is a general downward trend for E_gs above 1.8 eV.

Wider E_g perovskites in the range between 1.65 eV and 2.3 eV are most often achieved by the substitution of iodide with bromide. In such mixed bromide-iodide systems, the widely reported light- or electrical-bias-induced phase segregation presents an additional obstacle.[32–35] While the addition of a small amount of bromide has been shown to be beneficial for solar cell performance,[20,36] it has been widely assumed that chemical instability upon the addition of large amounts of bromide plays a role in the sublinear increase of V_{OC} loss with E_g.[28,37–39] However, in the case of mixed halide perovskites, several interconnected effects can affect the device's performance. To single out the most important cause of loss in performance, it is necessary to differentiate between voltage losses in the pristine, still mixed material due to quenching at either transport materials or material defects and on the other hand, voltage losses due to dynamic effects such as light-induced phase segregation.

Three dominant effects have been discussed:

- non-radiative recombination in the bulk
- non-radiative recombination due to transport materials
- phase segregation leading to:
  - Trapping of charge carriers in compositional inhomogeneities
  - Voltage pinning due to said compositional inhomogeneities

We here set out to discuss these three effects and their role in the observed losses in V_{OC} and J_{SC} in wide E_g perovskites, between 1.6 and 2.2 eV.

3.1. Performance Losses Due to Halide Composition

To evaluate the role that the halide composition plays on the solar cell metrics, the bromide content, $x = \frac{Br}{Br+I}$, was extracted for all devices in the database. We report here the *nominal* composition, as it is commonly defined, that is, by reporting the ratios of salts/halides in the perovskite inks. The compositional range was discretised in steps of $\Delta x = 0.01$. For a meaningful comparison of the device parameters for different E_gs, we perform our analysis relative to the SQ-limit.[27] $V_{OC,\,SQ} - V_{OC}$ is shown in **Figure 3a**. $V_{OC,\,SQ} - V_{OC}$ gives a direct measure of the voltage loss compared to the radiative limit and is not directly E_g-dependent.[27] A smaller voltage loss is favourable and signifies smaller deviations from the theoretical optimum. To evaluate the dependence of the J_{SC} on the composition, we normalised the J_{SC} by the maximal short circuit current obtainable according to the SQ-limit ($J_{SC,\,SQ}$) for each E_g, as shown in Figure 3b. Cells with a $V_{OC,\,SQ} - V_{OC} = 0$ or $J_{SC}/J_{SC,\,SQ} > 1$ were excluded from this analysis. In these cases, either the V_{OC} or J_{SC} is overestimated, or the E_g is determined inaccurately. A detailed account of the influence of the E_g determination on overreporting can be found in the Supporting Information, S1, and ref. [40]. Next to the reported data, both the average value (circles) and the average of the best 10% (stars) for each compositional subrange were calculated to guide the eye through the data cloud. We deem the average of the top-performing 10% of reported cells of each compositional subrange to be a good indicator of the state-of-the-art high-performance perovskite solar cells without a mere focus on individual record devices. The number of devices reported for each compositional subrange is given by the colour in Figure 3a,b. Next to pure iodide devices, devices with a bromide content of $x = 0.1$ to 0.2 make up a large portion of the reported devices. The addition of small amounts of bromide indeed improves solar cell performance. The V_{OC} loss for the best-performing devices decreases from 200 mV for pure iodide devices to 150 mV. Similarly, the J_{SC} for the top 10% of devices increases from 90% of the radiative limit to 95% for devices with a bromide content of $x = 0.3$.

Upon the addition of more bromide, both the J_{SC} as well as the V_{OC} start to deviate significantly from the SQ-limit. The $V_{OC,\,SQ} - V_{OC}$ of the average cells, as well as for the top 10%, is continuously increasing up to a bromide fraction of $x = 0.7$. For even higher bromide contents, a very sharp increase in V_{OC} loss can be seen, coincidental with a severe lack of reported devices. Devices around $x = 0.9$ show a 600–800 mV voltage loss for both the mean value and the top 10% of devices, compared to 400 mV (200 mV) for the average (top 10%) of the pure iodide counterparts. Similarly, the $J_{SC}/J_{SC,\,SQ}$ decreases continuously for bromide contents between $x = 0.4$ and $x = 0.6$ and then sharply declines for bromide contents above $x = 0.6$. At $x = 0.9$, the $J_{sc}$of the average cells (top 10%) is as low as 40% (70%) of the theoretical limit. It is remarkable, however, that despite the low quality of high bromide devices, pure bromide devices perform similarly to pure iodide devices. Especially, the top-performing pure bromide solar cells show a significantly smaller voltage loss than devices

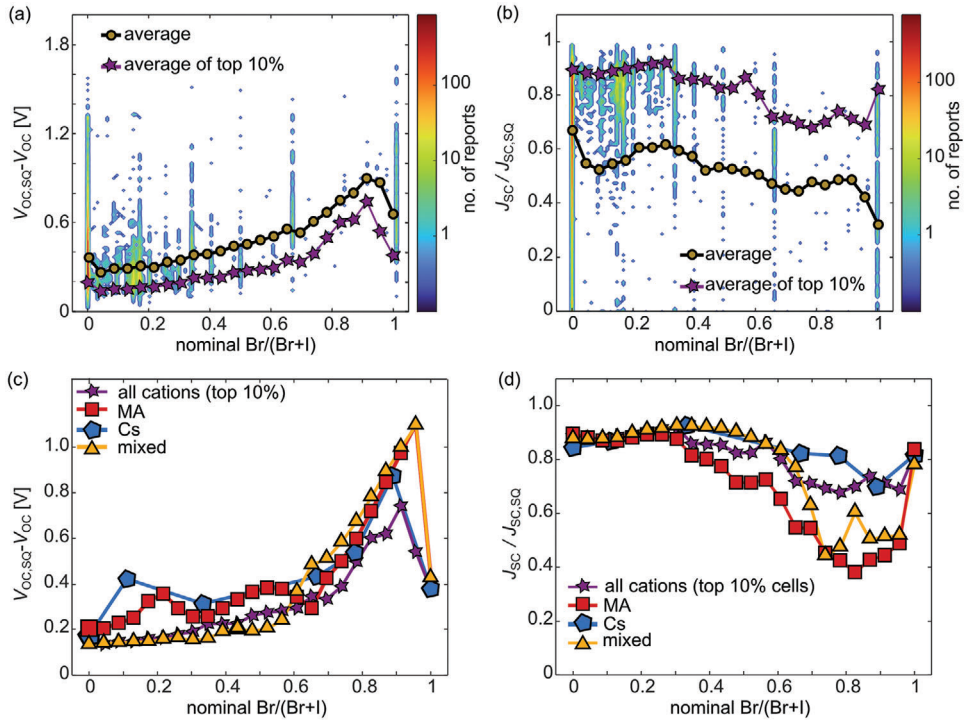

Figure 3. Comparison of the device performance depending on the nominal Br/(Br+I) composition. a) The dependence of $V_{OC,\,SQ} - V_{OC}$ on the composition Br/(Br+I) shows the previously reported increase in voltage loss for higher bromide contents and a sharp decrease of the loss for pure bromide samples. The circles show the mean of all devices, while the stars show the mean of the top 10% of the devices. b) Similarly, the $J_{sc}/J_{SC,\,SQ}$ shows a decrease in current for bromide contents above 0.3 and a sudden increase in current for the pure bromide devices. c) The same general behavior of $V_{OC,\,SQ} - V_{OC}$ can be seen independent of the cation. d) The cation dependence of $J_{SC}/J_{SC,\,SQ}$ shows that the general tendency of a decreased current at high bromide contents is independent of the cation. However, mixed cation devices show an initial increase in the current up to bromide contents of 0.4–0.5 and only a decline at even higher bromide contents.

with a small fraction of iodide. In $J_{SC}/J_{SC,\,SQ}$, the remarkable increase in the top-performing pure bromide cells is obvious. For the top 10%, $J_{SC}/J_{SC,\,SQ}$ is almost at the same level as for the pure iodide cells (85%). Nonetheless, the average cells only show a $J_{SC}/J_{SC,\,SQ}$ of around 30%. This large difference between the behaviour for the top 10% and the average cells indicates that optimising the intrinsic material property and the entire layer stack is a major issue, especially for the high bromide cells.

Comparing the cation-dependence of the top 10% of reported devices (Figure 3c,d) shows that the general behaviour of the solar cell performance upon the addition of bromide, consisting of an initial increase upon the addition of small fractions of bromide, followed by a continuous decrease upon further addition of bromide, a collapse of the solar cell performance for very high bromide contents and a nearly complete recovery for pure bromide devices is cation independent. Beyond this general trend, also distinct differences can be seen. In $J_{SC}/J_{SC,\,SQ}$ significant differences can be seen in the narrow-E_g region (Figure 3d). In the MA-system, $J_{SC}/J_{SC,\,SQ}$ benefits hardly at all from the addition of bromide and already declines at bromide fractions above $x = 0.25$. In contrast, in mixed cation systems, the highest $J_{SC}/J_{SC,\,SQ}$ can be seen in devices with a fraction of bromide around $x = 0.4$ and a sharp decline only starts at bromide fractions above $x = 0.5$. Additionally, in the Cs-system, the decline seems to be much less severe than in all other systems.

The clear increase in performance for pure bromide devices is obvious in all cation systems. This remarkable difference between almost pure bromide devices and pure bromide devices shows that the increased losses in both $J_{SC}/J_{SC,\,SQ}$ and $V_{OC,\,SQ} - V_{OC}$ observed for mixed halide perovskites are at least in part connected to the halide composition and not purely to the E_g. Notably, the shallow increase in losses for both V_{OC} and J_{SC} upon increasing the bromide ratio may also stem from an increased excitonic loss, yet cannot explain the abrupt behaviour when moving from $0.7 < x < 1$ to $x = 1$.

3.2. Most Common Transport Materials

The primary focus of perovskite research has been on pure iodide or almost pure iodide compositions, with over 30,000 devices reported in the E_g range 1.5–1.6 eV, that is, $FAPbI_3$ - $MAPbI_3$. Accordingly, many *optimised* transport materials are optimised for that E_g range, which likely leads to misalignment with other MHPs in other E_g ranges. We here discuss the role of misaligned transport materials in wide E_g perovskites. Looking at the E_g-dependent use of the most common hole-transporting materials (HTMs) and electron-transporting materials (ETMs), as shown in **Figure 4**, gives an overview of the state of layer stack optimisation apart from the 1.6 eV perovskites. As over 1,800 different HTMs were reported, we categorised them according to the material in

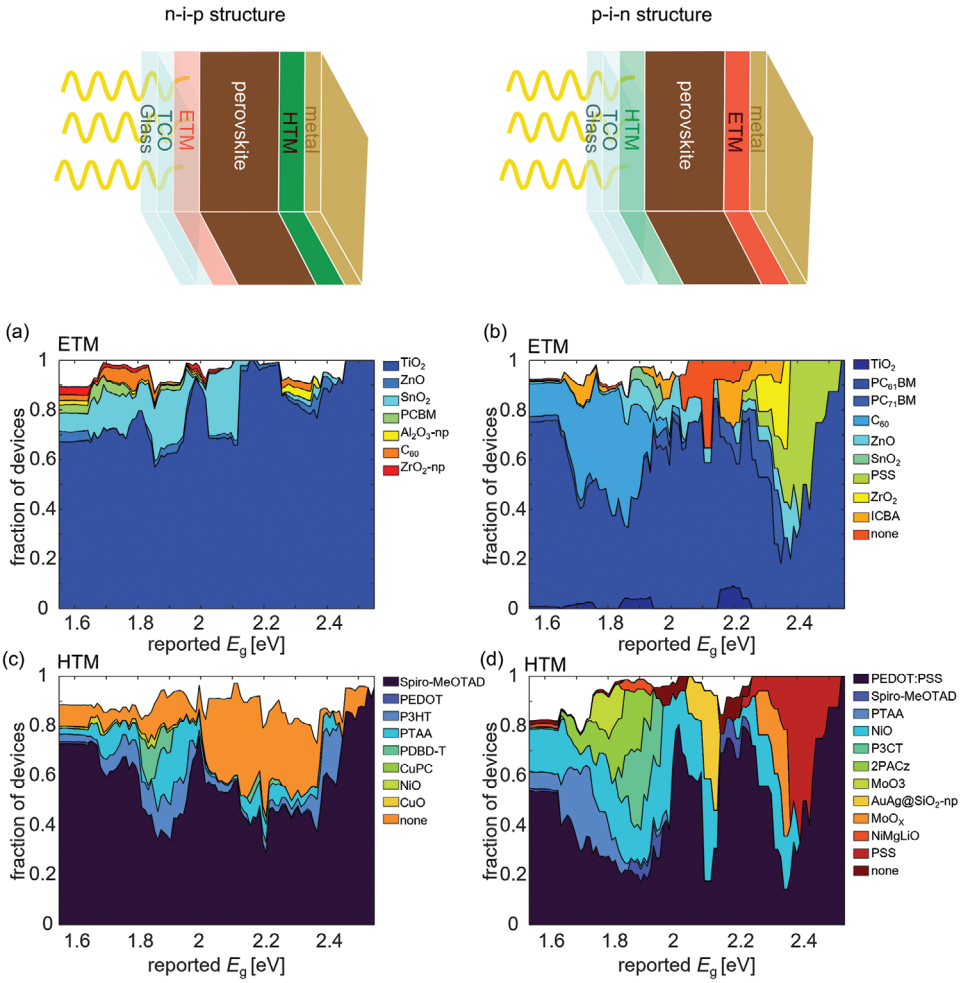

Figure 4. Analysis of most commonly utilised ETMs and HTMs used in wide E_g MHP-based solar cells. a) and b) show the most common ETMs in the n-i-p and p-i-n configurations, respectively, b) whereas c) and d) show the most common HTMs of the of n-i-p and p-i-n configurations. For each device, the layer in contact with the perovskite is chosen. The bandgap range from 1.55 to 2.5 eV is discretized in 100 subranges to determine the most common material for each bandgap subrange. 'none' signifies that no HTM or ETM was used in the device stack.

direct contact with the perovskite. We show the most commonly used transport materials separately for n-i-p and p-i-n structures in Figure 4. Especially in n-i-p structures, it can be seen that despite the large E_g range, most of the devices were prepared with the same ETMs and HTMs (Figures 4a and 4c). TiO_2 and Spiro-MeOTAD are still the most prominent transport materials across the entire E_g range, with TiO_2 being used in more than 50% of devices at all E_gs. TiO_2 and Spiro-MeOTAD coincidentally fit reasonably well with the archetypal $MAPbI_3$ perovskites, probably a major contribution to the success of initial perovskite devices. However, at deviating E_gs, the energy levels are mismatched such that a significant portion of the decrease in cell performance for wide E_g cells can be explained by energy level misalignments with the transport materials. Remarkably, in close to 40% of the n-i-p cells with E_gs between 2.0 eV and 2.4 eV, no HTM was used.

In p-i-n structured devices, more diversity of transport materials can be seen. ETMs are clearly dominated by C_{60} and its derivatives, such as $PC_{61}BM$ and $PC_{71}BM$. Especially at E_gs between 1.6 and 2 eV, above 80% of devices rely on C_{60}-derived ETMs. Only at E_g,s above 2.0 eV, do other materials such as ICBA, ZrO_2, and PSS gain relevance. The HTMs show even stronger E_g-dependence, with more E_g range-specific materials.

3.3. Performance Losses Due to Energetic Misalignment with Transport Materials

To evaluate the effect of the misalignment of transport materials on the device performance, we here take a closer look at devices containing C_{60}-derived ETMs and PTAA as HTM. The rearrangement of mobile ions impacts the electrostatics of devices containing halide perovskites under working conditions. Yet, the simplest manifestation—that is, an accumulation of ions at the interfaces and hence a lowering of the effective field across the bulk, accentuates fundamental considerations regarding the alignment of energy levels at a given perovskite/transport material interface as they reduce the positive effect of any built-in electric field. As the database currently does not contain any information about the energetics of the perovskites or the transport materials employed, direct correlations between recombination

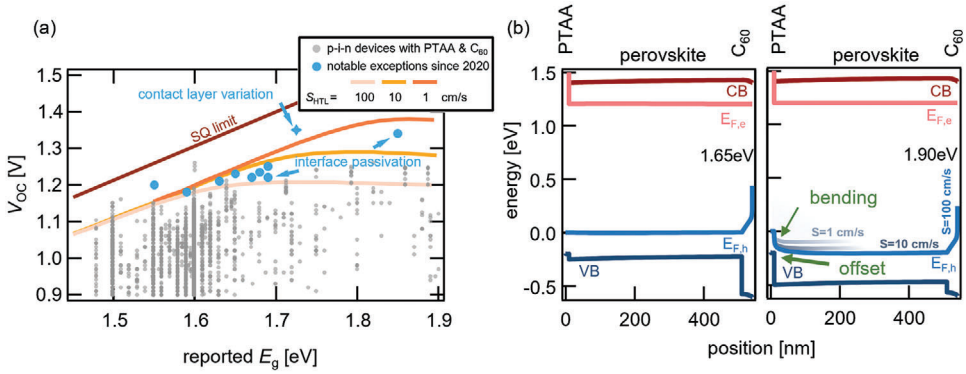

Figure 5. a) Open-Circuit Voltage (V_{OC}) of selected p-i-n devices with fixed transport materials (undoped PTAA & C_{60}) for reports with different E_gs (grey circles). The blue symbols indicate notable exceptions from the last two years (circles with analogous TLs), benefitting from interface passivation, while the blue star represents an analogous sample where the ETM layer was varied. The full lines correspond to the SQ-limit (maroon) and drift-diffusion simulations with varying surface recombination velocities at the HTM/perovskite interface (orange shading). b) Band diagram of a 1.65 eV (left) and 1.90 eV perovskite solar cell with fixed transport materials (undoped PTAA & C_{60}). In the 1.90 eV case, there is significant bending of the hole quasi-Fermi level ($E_{F,h}$) at the PTAA/perovskite interface due to the large offset (both indicated in green). This bending is reduced upon reducing the surface recombination velocity (blue shadings).

losses and energetic offsets are not available a priori. However, the dataset allows the selection of a subset of solar cells with fixed properties. **Figure 5** presents the reported V_{OC}s of such a subset of p-i-n devices with fixed transport materials (PTAA and C_{60}, as HTM and ETM, respectively). The selection of this subset is motivated by the fact that this layer stack is currently most commonly used in the fabrication of perovskite/silicon tandems, where E_g tunability is of particular interest. In Figure 5a, notably, the V_{OC} of these devices appears to plateau above E_g = 1.65 eV at approximately 1.21 V. This coincides with the range of E_gs, which are reported to exhibit a phase-instability under illumination, so it may appear intuitive to assume that this is the origin of this plateauing. However, this is not the only explanation. A more straightforward explanation is given when considering the interplay between energetic offsets (that must occur) when changing only one of the constituents and a varying degree of interfacial recombination (often quantified in the form of a surface recombination velocity, S). Based on experimentally validated input parameters, we made drift-diffusion simulations of the stack mentioned above with the software SCAPS-1D.[41–43] For this purpose, we varied only two parameters: the E_g of the perovskite (through changing the ionisation potential with fixed electron affinity, that is, shifting the valence band) and the recombination at the perovskite/HTM interface by varying the number of available traps to facilitate recombination at this interface, resulting in a set with S = (100, 10, 1 cms $^{-1}$), respectively.

These simulation results are shown in Figure 5a as solid lines in different shades of orange. In the range between S = 10 to 100 cm s^{-1}, the model appears to capture the situation in the best devices quantitatively well (grey dots, i.e., highest V_{OC} reported), including the plateau. The same effect would be observed if the conduction band and the recombination at the perovskite/ETM interface were modulated.

The other simulations (S = 1 cm s^{-1}) can be considered as guides on how to reduce recombination and hence increase V_{OC} for wide E_g devices (E_g > 1.65 eV), that is, by reducing the surface recombination velocity or reducing the number of available carriers involved in the vicinity of the interface (energetic alignment, better minority carrier repulsion). This would allow for higher V_{OC}s at wider E_gs and a shift of the onset of the plateau to wider E_gs. These are precisely the strategies employed in the reports indicated as "notable exceptions" in Figure 5a. The most significant part of these devices showed a reduction of surface recombination in bilayers with transport materials (blue circles) or a reduction of energy offset by varying the transport material (blue asterisk, the devices from **Figure 6c**). To better understand this phenomenon, we also visualized the band diagrams of these simulated devices at open circuit in Figure 5b for the almost perfectly aligned (1.65 eV) and the highly misaligned (1.90 eV) case. In the latter case, one observes a reasonably large offset between the valence band of the perovskite and the HOMO level of the PTAA. This, in turn, results in significant recombination at the interface, which results in a strong bending of the hole quasi-Fermi level ($E_{F,h}$) and pins the achievable V_{OC}, albeit the bulk would allow for a significantly higher V_{OC}s (approximately 0.15 eV difference between μ in the bulk vs. at the contacts). Upon reducing surface recombination at the limiting interface, the bending is reduced but not eliminated (HTM in this case, blue shading) even if this recombination is entirely suppressed (S = 0 cm s^{-1}). However, this resolves only the loss under flat band conditions, that is, at open-circuit, while at working voltages $V < V_{OC}$, the bending would still occur, resulting in a significant fill factor (FF) penalty. This underlines the importance of energetically aligned transport materials to maximize the V_{OC}, FF and, consequently, efficiency when tuning the E_g for wide E_g devices.

Two examples showing the importance of adjusting the interface between a wide E_g and the transport layer are the works from Liu et al. and Chen et al., shown in Figure 6a–c.[44,7]

Chen et al. perform a detailed loss analysis of the V_{OC} of a $Cs_{0.2}FA_{0.8}Pb(I_{0.6}Br_{0.4})_3$ device with a bandgap of 1.79 eV, shown in Figure 6a,b. The results demonstrate the potential of passivating the interface between the electron transport layer (ETL) and the perovskite in wide-band gap devices. While untreated films report a 100 mV loss due to the interface, treating the interface with PDA reduces this loss by a factor of five to only 20 mV. This reduces carrier trapping and improves carrier extraction.[44]

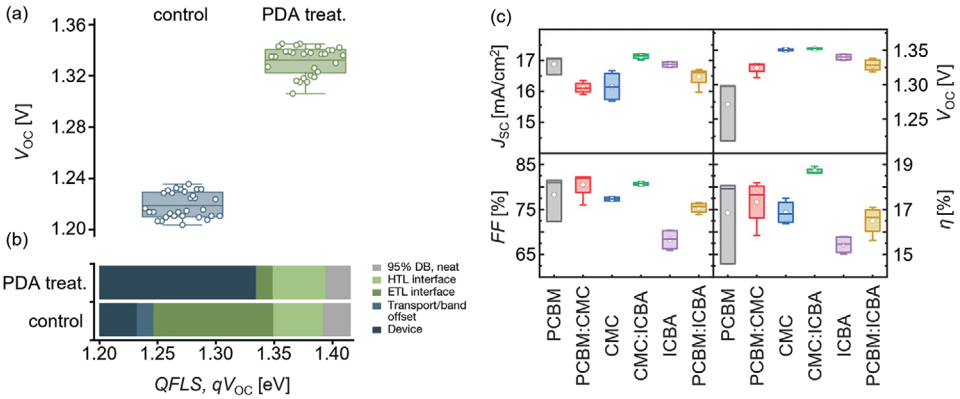

Figure 6. Examples of two approaches to enhance the V_{OC} in devices utilizing C_{60} derived transport materials. a) and b) Show how, with PDA treatment, the V_{OC} loss at the ETM interface can be drastically reduced. Reproduced with permission.[44] Copyright, Springer Nature, 2023. c) Device performance of ITO/PTAA/$MAPb(I_{0.8}Br_{0.2})_3$/ETM/BCP/Ag solar cells with high V_{OC}s of up to 1.35V. Device parameters of the solar cells are compared for different C_{60} derived ETMs given on the x-axis. Note that PCBM has the highest electron affinity in the series, with ETMs involving CMC and ICBA generally having lower electron affinities. The ETMs with higher electron affinities generally have lower V_{OC} values. In comparison, combinations with lower electron affinities have higher V_{OC} but, in some cases, also lower *FF*s. In this particular case, a blend of CMC and ICBA led to the best compromise between *FF* and V_{OC} suggesting that the fine-tuning of interface properties can have a significant effect on device performance, in particular for absorber materials with somewhat wide E_gs (such as 1.72 eV in this case). Reproduced with permission.[7] Copyright, the authors, 2021.

Through this treatment, a V_{OC} of 1.33 V at a bandgap of 1.79 eV is achieved, which corresponds to a surface recombination velocity, S, of about 1 cm s^{-1}, as obtained from the SCAPS simulation shown in Figure 5a. Liu et al. increased the E_g of a highly luminescent $MAPbI_3$ recipe based on lead-acetate[22] by adding 20% bromide leading to a E_g of 1.72 eV, that is, close to the ideal E_g for tandem applications. While the pure $MAPbI_3$ led to a V_{OC} of 1.26 V at 1.6 eV E_g with PTAA and PCBM as hole and electron transport material, it was initially not possible to increase the V_{OC} in parallel with the E_g increase. Therefore, the authors optimized the electron transport material by using fullerenes (i.e., C_{60} derivatives) with lower electron affinities. The optimized recipe at the end involved a mixed fullerene layer based on ICBA (indene-C_{60} bisadduct) and CMC (C_{60}-fused N-methylpyrrolidine-m-C_{12}-phenyl) that led to a V_{OC} of 1.35 V at a 1.72 eV E_g as shown in Figure 6c. Thus, the voltage loss relative to the SQ-limit (1.42 V) had gone up by only 10 mV (≈60 mV for $MAPbI_3$ and ≈70 mV for $MAPb(I_{0.8}Br_{0.2})_3$). This result shows that at least for bromide concentrations up to 20%, no fundamental reason would forbid high bulk quality. The challenge, however, is to find suitable charge-transport materials. The downside of ICBA and CMC is their slightly lower mobility, which is detrimental to charge extraction, thereby limiting overall efficiency. As long as inverted perovskite solar cells stick with fullerenes as ETMs, this may become a fundamental problem for wide E_g perovskites. Significantly lower electron affinities than PCBM can often only be obtained using fullerene multiadducts like ICBA.[45] Fullerene multiadducts; however, are known to increase disorder and decrease electron mobility.[46,47]

The mismatch of energy levels between the MHPs and the transport materials is expected to show a continuous decrease in device performance with increasing deviation from the standard E_g of 1.6 eV, to which most transport materials are optimized. The nearly linear increase in V_{OC} loss can, therefore, be explained by an increased mismatch between the absorber and transport materials. This conclusion is especially corroborated by the recent examples defying this trend by diligent optimization of the device stack.

Beyond the continuous decrease at E_gs between 1.6 and 1.8 eV, the sudden collapse of device performance for very high bromide contents above $x = 0.5$ and the abrupt increase of device performance for the top performing pure bromide cells (shown in Figure 3) cannot be explained with a pure mismatch phenomenon. Especially the stark difference between devices with a high bromide content (x ≈ 0.9) and the pure bromide devices pinpoints to the halide mixture itself to play a significant role in the reduced V_{OC}.

3.4. Non-Radiative Recombination

Non-radiative recombination is detrimental to the efficiency of solar cells, as it decreases the number of charge carriers to be extracted and, even more so, the potential work they can deliver, in consequence, the V_{OC}. Non-radiative bulk recombination typically occurs from the conduction band via defects in the E_g to the valence band. Lead halide perovskites have been shown to be 'defect-tolerant', meaning that shallow intrinsic defects are much more likely than deep intrinsic defects. It is so far still an open question whether deep or shallow defects eventually dominate the recombination, and it could very well depend on the type of perovskite and the preparation process. No matter whether it is a small density of deep defects or a (possibly higher) density of shallow defects that dominates recombination, it should be significantly less detrimental as compared to many other polycrystalline semiconductors. This is mainly due to shallow defects having typically lower capture coefficients for the capture of either electrons or holes.[48] In contrast, deep defects are more likely to capture electrons and holes equally well. Thus, a given density of shallow defects is expected to have a reduced impact on the luminescence quantum efficiency relative to the same density of deep defects. In perovskites with a E_g around 1.6 eV, the external

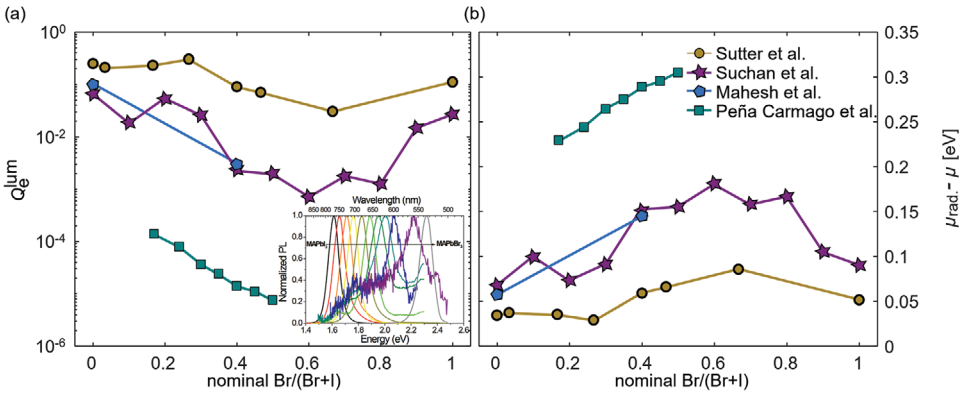

Figure 7. a) shows that the Q_e^{lum}, as reported in the literature, reduces with higher bromide fractions. However, the pure bromide samples show a Q_e^{lum} close to that of the pure iodide samples. The inset shows that even in one of the earliest measurements of the PL for varying bromide fractions, this dependency is apparent in the noise level. b) Shows the non-radiative loss ($\mu_{rad.} - \mu$) as calculated from the reported Q_e^{lum}.

photoluminescence quantum yield (PLQY, Q_e^{lum}) has repeatedly been reported around and even above 10%.[29,49,50]

However, for mixed bromide-iodide perovskites, the Q_e^{lum} has been reported to be reduced.[29,49,51] Already in the first report of phase segregation in mixed bromide-iodide perovskites by Hoke et al., it became clear that the Q_e^{lum} of pristine films, prior to segregation is dependent on the bromide content.[32] This can be seen in increasingly noisy spectra in the inset of **Figure 7a**. Only the pure bromide sample has a reduced noise again. As the database focuses on device metrics rather than fundamental material properties, Q_e^{lum} is not yet included in the database. We instead rely on individually reported Q_e^{lum} datasets and our original data. More information concerning the original data can be found in the Supporting Information.

In Figure 7a, the Q_e^{lum} is shown for varying bromide contents x. It becomes clear that the Q_e^{lum} decreases with the bromide content to values as low as 0.3–1%. However, for the pure bromide perovskites, the Q_e^{lum} recovers to values as high as 5–10%, similar to that of pure iodide perovskites. Such a drop in the luminescence quantum efficiency Q_e^{lum} can be directly correlated to a loss in the achievable Quasi-Fermi-Level-Splitting (μ, *QFLS*) through refs. [52,53]:

$$\mu_{rad.} - \mu = -k_B T \ln [Q_e^{lum}] \quad (1)$$

The non-radiative loss, shown in Figure 7b, shows that an additional loss of approximately 100 meV in high bromide samples can be expected purely due to an increase in non-radiative recombination that may originate, for instance, from an increased defect density.

An astonishing factor in this context is the sharp increase of the Q_e^{lum} for the pure bromide samples, which reach values that are only slightly lower than the pure iodide samples (15% Richter et al., 5% Suchan et al., and 12% Sutter-Fella et al.).[49,54,55] This composition-dependent behaviour of the Q_e^{lum} indicates that the decrease in Q_e^{lum} in the mixed samples must be an effect directly connected to the mixture. This could be defects due to lattice inhomogeneity due to the size difference of the ions or pre-existing chemical inhomogeneity. Qualitatively, this composition-dependent behaviour of the Q_e^{lum} agrees surprisingly well with the behaviour of both J_{SC} and the V_{OC} loss of the top performing devices, shown in Figures 3a and 3b.

While 100 meV is a significant loss that will become very relevant for optimized solar cells, it is still far from explaining the observed additional loss of roughly 500 mV in devices with $x = 0.9$.

3.5. Phase Segregation

Besides the discussed losses in pristine devices, light-induced compositional instability is a necessary factor to consider when evaluating the solar cell performance of mixed (I, Br) metal halide perovskites. The light-induced phase segregation of mixed halide perovskites has been widely discussed after a first report by Hoke et al.[32] In a first step upon illumination, nano-sized iodide-rich domains form. These newly formed iodide-rich domains have a smaller E_g than the surrounding mixed material. Thus, it has been observed that nearly all charge carriers funnel into the newly emerging iodide-rich domains. This charge carrier funnelling is thought to stabilize the iodide-rich domains and even lead to continuous phase segregation in a second stage.

The formation of a low E_g phase has been shown to lead to voltage pinning at the lowest energy phase.[28,53] V_{OC} losses of 70–130 mV have been reported.[56,57] With that, it can explain a fraction of the observed increased V_{OC} loss for devices with higher bromide content. Mahesh et al.[29] conclude that this surprisingly small V_{OC} loss related to phase segregation is due to two effects counteracting each other. The effect of the voltage pinning occurring due to segregation can be reduced if the luminescence quantum efficiency of the narrower E_g material is significantly higher than that of the mixed material. Beyond this phase, segregation has been shown to have an even stronger effect on the J_{SC} with a decrease of over 80% of the initial value. The newly formed isolated iodide-rich domains may act as trap states reducing J_{SC}.[56,57] A summary of the in-situ reports, tracking the evolution of V_{OC} and J_{SC} during phase segregation is shown in Figure S3, Supporting Information.[29,56–58] The experimental evidence thus clearly shows that phase segregation is detrimental for the solar cell performance.

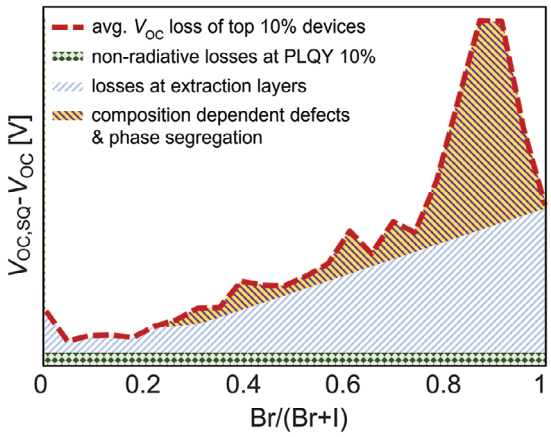

Figure 8. Cartoon indicating the dependence of the contribution of different loss mechanisms to the overall observed loss in V_{OC} on the bromide content.

In such a chemically unstable material, reported *JV* curves result from a mixture of pristine effects, such as the layer stack and the intrinsic material properties, as well as dynamic effects, such as phase segregation, light soaking, degradation and hysteresis. In reported *JV* curves, it is often still unclear how long the sample has been illuminated or bias (and under which conditions) prior to the measurement, such that only a convoluted effect is visible.

Furthermore, it is noteworthy that not only the Q_e^{lum} but also the reported composition-dependent chemical photo-stability follows the same dependence on the halide composition as the herein reported V_{OC} loss and J_{SC}.[35] The instability of mixed halide perovskites with compositions of $x > 0.2$ has been shown to increase with bromide content gradually and exhibits a maximal instability at $x = 0.9$ when only a small fraction of iodide is added to pure bromide perovskites, reproduced in Figure S4b, Supporting Information.[35] This qualitative agreement between device performance, the pristine material quality and the chemical photo-stability pinpoints an interconnecting effect. Pre-existing defects impacting the Q_e^{lum} may as well be templating the phase segregation, which is mainly dependent on defect concentration.[35,59–61] Vice versa Peña-Carmargo et al. pointed out that initial phase segregation at a very low level may appear as increased defect density,[51] such that the apparently increased defect density in bromide-rich samples could also be a disguised initial phase segregation. This highlights that defect density and chemical instability cannot be viewed as two disconnected topics but are highly correlated.

3.6. Rating of Performance Losses of Wide Bandgap Metal Halide Perovskite Solar Cells

After considering the different loss mechanisms and their effect on the E_g and composition-dependent device performance, we can conclude that not a single mechanism can be deemed responsible for the entirety of the voltage losses observed in wide E_g perovskites. However, for different E_gs and composition regions, different mechanisms may be dominant, as indicated in **Figure 8**.

The losses at the transport material interfaces are expected to be dependent on the band offset, increasing continuously with energetic distance from the band energy for which the layer stack was optimised. In most cases, the layer stack has been optimised for a 1.6 eV pure or almost pure iodide perovskite as the absorber layer. Losses at transport materials due to interface recombination or band-misalignment can be assumed to be the dominant loss mechanism at moderate bromide concentrations with E_gs up to 1.8 eV. Recent breakthroughs[44,62] showcase that diligent optimisation for this specific E_g range may lead to high-quality perovskite devices with a low voltage loss of around 60 mV for a E_g up to 1.75 eV. This shows that layer stack optimisation and finding proper transport materials is the main challenge to developing efficient wide bandgap cells.

Higher bromide contents are needed for even wider E_gs, which adds additional complication through chemical instability and inhomogeneity. Above a bromide content of $x = 0.5$, the device performance is nearly collapsing. The light-induced phase segregation and decreased Q_e^{lum} set in in this range, which may cause this performance collapse. The stark difference between mixed devices with a high bromide content ($x \approx 0.9$) and the pure bromide devices points to phase segregation playing a significant role in the reduced V_{OC}, which has been shown to have a similar abrupt onset.[35] Thus, high-performance perovskite films in this region, which are of importance for perovskite-perovskite, perovskite-III-V tandems as well as green perovskite LEDs, require further work to understand the connection between phase segregation and defect density.

4. Conclusion

The comparison of the over 45,000 experimental datasets on the efficiency of metal halide perovskite solar cells enables us to draw generalised conclusions regarding the current limits of their device performance. We compared and discussed the effect of both intrinsic and optimisation limitations, including suboptimal band alignment, poor absorber quality, and chemical instability, on the device performance.

While perovskite devices with increasingly diverse E_gs were developed throughout the years, by now spanning the whole range between 1.2 eV and 3 eV, the material quality is not necessarily optimal for the entire E_g range. The best-performing solar cells are still obtained with structures close to the $MAPbI_3$ archetype with E_gs between 1.55 eV and 1.6 eV., which is likely due to the dominant effort in optimising devices for MHP absorbers in this E_g range.

The performance discrepancy between the theoretical limit of wide E_g MHP semiconductors is, as discussed in this work, a consequence of substantially less effort in optimising/matching selective transport materials for wide E_g MHP solar cells, but also a lower optoelectronic quality of wide E_g MHPs due to non-optimised layer fabrication as well as dynamically established phase-inhomogeneity that leads to performance losses.

Overall, viewing a large number of experimental datasets on perovskite device efficiency in direct comparison shows the tremendous progress in metal halide perovskites in recent years. Supporting Information: Additional details on the distribution of bandgaps in the analysed datasets, a detailed discussion of challenges in accurate bandgap determination, a discussion of the evolution of device metrics during operation as well as a brief discussion of certified devices.

Supporting Information

Supporting Information is available from the Wiley Online Library or from the author.

Acknowledgements

E.L.U. and K.S. acknowledge financial support from the Swedish Research Council (Grant Nos. 2015-00163 and 2018-05014) and Marie Sklodowska Curie Actions, Cofund, Project INCA 600398 and Nano Lund. E.L.U. and C.R. would also like to acknowledge financial support from the German Federal Ministry of Education and Research (BMBF–NanoMatFutur Project HyPerFORME: 03XP0091). C.R. acknowledges financial support from the HI-SCORE Research School of the Helmholtz Association. C.M.W. acknowledges funding from the European Union's Horizon 2020 research and innovation program (VIPERLAB, 101006715; TRIUMPH, 101075725), the Swiss National Science Foundation (PAPET, 200021_197006; A3P, 40B2-0_1203626), the Swiss Federal Office of Energy (PRESTO, PERSISTARS), and the ETH Domain through an AM grant (AMYS). T.J.J. acknowledges the Ministry of Science and Technology in China via the National Key Research and Development Program of China (Grant No. 2021YFF0500501), and Applied Basic Research Projects in Tianjin (Grant No. 22JCYBJC01530).

Conflict of Interest

The authors declare no conflict of interest.

Data Availability Statement

The data is acquired from the Perovskite Database Project, which is described in Nature Energy (https://doi.org/10.1038/s41560-021-00941-3). The most up-to-date dataset can be downloaded from https://www.perovskitedatabase.com.

Keywords

database, higher bandgap, metal halide perovskite, open circuit voltage

Received: October 10, 2023
Revised: November 18, 2023
Published online: December 15, 2023

[1] C. H. Henry, *J. Appl. Phys.* **1980**, *51*, 4494.
[2] A. Martí, G. L. Araújo, *Sol. Energy Mater. Sol. Cells* **1996**, *43*, 203.
[3] T. Kirchartz, U. Rau, *Adv. Energy Mater.* **2018**, *8*, 1703385.
[4] G. E. Eperon, M. T. Hörantner, H. J. Snaith, *Nat. Rev. Chem.* **2017**, *1*, 0095.
[5] T. Leijtens, K. A. Bush, R. Prasanna, M. D. McGehee, *Nat. Energy* **2018**, *3*, 828.
[6] L. Schmidt-Mende, V. Dyakonov, S. Olthof, F. Ünlü, K. M. T. Lê, S. Mathur, A. D. Karabanov, D. C. Lupascu, L. M. Herz, A. Hinderhofer, F. Schreiber, A. Chernikov, D. A. Egger, O. Shargaieva, C. Cocchi, E. Unger, M. Saliba, M. M. Byranvand, M. Kroll, F. Nehm, K. Leo, A. Redinger, J. Höcker, T. Kirchartz, J. Warby, E. Gutierrez-Partida, D. Neher, M. Stolterfoht, U. Würfel, M. Unmüssig, et al., *APL Mater.* **2021**, *9*, 109202.
[7] J. Liu, J. Qu, T. Kirchartz, J. Song, *J. Mater. Chem. A* **2021**, *9*, 20919.
[8] M. A. Green, E. D. Dunlop, M. Yoshita, N. Kopidakis, K. Bothe, G. Siefer, X. Hao, *Prog. Photovolt. Res. Appl.* **2023**, *31*, 651.
[9] W. Shockley, H. J. Queisser, *J. Appl. Phys.* **1961**, *32*, 510.
[10] We would like to note that we discussed describing the theoretical limit calculated by Shockley and Queisser using different terminology but, for the lack of better terminology, decided not to. The racist and eugenicist views of William Shockley are undisputed, yet the now often-used alternative names "detailed balance limit", "thermodynamic limit", or "radiative limit" lack specificity. The SQ-limit constitutes one specific case among the set of radiative or thermodynamic efficiency models and obeys the principle of detailed balance like many other models as well (incl. the Shockley-Read-Hall recombination model). However, these are not mutually exclusive definitions, cf., all elephants are animals, not all animals are elephants.
[11] X.-K. Liu, W. Xu, S. Bai, Y. Jin, J. Wang, R. H. Friend, F. Gao, *Nat. Mater.* **2020**, *20*, 10.
[12] A. Dey, J. Ye, A. De, E. Debroye, S. K. Ha, E. Bladt, A. S. Kshirsagar, Z. Wang, J. Yin, Y. Wang, L. N. Quan, F. Yan, M. Gao, X. Li, J. Shamsi, T. Debnath, M. Cao, M. A. Scheel, S. Kumar, J. A. Steele, M. Gerhard, L. Chouhan, K. Xu, X. gang Wu, Y. Li, Y. Zhang, A. Dutta, C. Han, I. Vincon, A. L. Rogach, et al., *ACS Nano* **2021**, *15*, 10775.
[13] M. V. Kovalenko, L. Protesescu, M. I. Bodnarchuk, *Science* **2017**, *358*, 745.
[14] N. K. Dutta, X. Zhang, *Optoelectronic Devices*, World Scientific, Singapore **2018**.
[15] M. Yamaguchi, F. Dimroth, J. F. Geisz, N. J. Ekins-Daukes, *J. Appl. Phys.* **2021**, *129*, 240901.
[16] M. A. Green, A. Ho-Baillie, H. J. Snaith, *Nat. Photonics* **2014**, *8*, 506.
[17] S. D. Stranks, H. J. Snaith, *Nat. Nanotechnol.* **2015**, *10*, 391.
[18] J.-P. Correa-Baena, M. Saliba, T. Buonassisi, M. Grätzel, A. Abate, W. Tress, A. Hagfeldt, *Science* **2017**, *358*, 739.
[19] A. K. Jena, A. Kulkarni, T. Miyasaka, *Chem. Rev.* **2019**, *119*, 3036.
[20] N. J. Jeon, J. H. Noh, W. S. Yang, Y. C. Kim, S. Ryu, J. Seo, S. I. Seok, *Nature* **2015**, *517*, 476.
[21] Y. Ogomi, A. Morita, S. Tsukamoto, T. Saitho, N. Fujikawa, Q. Shen, T. Toyoda, K. Yoshino, S. S. Pandey, T. Ma, S. Hayase, *J. Phys. Chem. Lett.* **2014**, *5*, 1004.
[22] Z. Liu, L. Krückemeier, B. Krogmeier, B. Klingebiel, J. A. Márquez, S. Levcenko, S. Öz, S. Mathur, U. Rau, T. Unold, T. Kirchartz, *ACS Energy Lett.* **2019**, *4*, 110.
[23] O. Almora, D. Baran, G. C. Bazan, C. Berger, C. I. Cabrera, K. R. Catchpole, S. Erten-Ela, F. Guo, J. Hauch, A. W. Y. Ho-Baillie, T. J. Jacobsson, R. A. J. Janssen, T. Kirchartz, N. Kopidakis, Y. Li, M. A. Loi, R. R. Lunt, X. Mathew, M. D. McGehee, J. Min, D. B. Mitzi, M. K. Nazeeruddin, J. Nelson, A. F. Nogueira, U. W. Paetzold, N.-G. Park, B. P. Rand, U. Rau, H. J. Snaith, E. Unger, et al., *Adv. Energy Mater.* **2021**, *11*, 2102526.
[24] S. Ishizuka, *Phys. Status Solidi a: Appl. Mater. Sci.* **2019**, *216*, 1800873.
[25] D. Kreikemeyer-Lorenzo, D. Hauschild, P. Jackson, T. Friedlmeier, D. Hariskos, M. Blum, W. Yang, F. Reinert, M. Powalla, C. Heske, L. Weinhardt, *ACS Appl. Mater. Interfaces* **2018**, *10*, 37602.
[26] T. J. Jacobsson, A. Hultqvist, A. Garcia-Fernandez, A. Anand, A. Al-Ashouri, A. Hagfeldt, A. Crovetto, A. Abate, A. G. Ricciardulli, A. Vijayan, A. Kulkarni, A. Y. Anderson, B. P. Darwich, B. Yang, B. L. Coles, C. A. Perini, C. Rehermann, D. Ramirez, D. Fairen-Jimenez, D. Di Girolamo, D. Jia, E. Avila, E. J. Juarez-Perez, F. Baumann, F. Mathies, G. S. Anaya-González, G. Boschloo, G. Nasti, G. Paramasivam, G. Martínez-Denegri, et al., *Nat. Energy* **2022**, *7*, 107.
[27] W. Shockley, H. J. Queisser, *J. Appl. Phys.* **1961**, *32*, 510.
[28] E. L. Unger, L. Kegelmann, K. Suchan, D. Sörell, L. Korte, S. Albrecht, *J. Mater. Chem. A* **2017**, *5*, 11401.
[29] S. Mahesh, J. M. Ball, R. D. J. Oliver, D. P. McMeekin, P. K. Nayak, M. B. Johnston, H. J. Snaith, *Energy Environ. Sci.* **2020**, *13*, 258.

[30] P. J. Dale, M. A. Scarpulla, *Sol. Energy Mater. Sol. Cells* **2023**, *251*, 112097.
[31] J. Jeong, M. Kim, J. Seo, H. Lu, P. Ahlawat, A. Mishra, Y. Yang, M. A. Hope, F. T. Eickemeyer, M. Kim, Y. J. Yoon, I. W. Choi, B. P. Darwich, S. J. Choi, Y. Jo, J. H. Lee, B. Walker, S. M. Zakeeruddin, L. Emsley, U. Rothlisberger, A. Hagfeldt, D. S. Kim, M. Grätzel, J. Y. Kim, *Nature* **2021**, *592*, 381.
[32] E. T. Hoke, D. J. Slotcavage, E. R. Dohner, A. R. Bowring, H. I. Karunadasa, M. D. McGehee, *Chem. Sci.* **2014**, *6*, 613.
[33] M. C. Brennan, A. Ruth, P. V. Kamat, M. Kuno, *Trends Chem.* **2020**, *2*, 282.
[34] K. Suchan, A. Merdasa, C. Rehermann, E. L. Unger, I. G. Scheblykin, *J. Lumin.* **2020**, *221*, 117073.
[35] K. Suchan, J. Just, P. Beblo, C. Rehermann, A. Merdasa, R. Mainz, I. G. Scheblykin, E. Unger, *Adv. Funct. Mater.* **2023**, *33*, 2206047.
[36] J. J. Yoo, G. Seo, M. R. Chua, T. G. Park, Y. Lu, F. Rotermund, Y.-K. Kim, C. S. Moon, N. J. Jeon, J.-P. Correa-Baena, V. Bulović, S. S. Shin, M. G. Bawendi, J. Seo, *Nature* **2021**, *590*, 587.
[37] X. Tang, M. van den Berg, E. Gu, A. Horneber, G. J. Matt, A. Osvet, A. J. Meixner, D. Zhang, C. J. Brabec, *Nano Lett.* **2018**, *18*, 2172.
[38] R. A. Belisle, K. A. Bush, L. Bertoluzzi, A. Gold-Parker, M. F. Toney, M. D. McGehee, *ACS Energy Lett.* **2018**, *3*, 2694.
[39] R. E. Beal, N. Z. Hagström, J. Barrier, A. Gold-Parker, R. Prasanna, K. A. Bush, D. Passarello, L. T. Schelhas, K. Brüning, C. J. Tassone, H.-G. Steinrück, M. D. McGehee, M. F. Toney, A. F. Nogueira, *Matter* **2020**, *2*, 207.
[40] L. Krückemeier, U. Rau, M. Stolterfoht, T. Kirchartz, *Adv. Energy Mater.* **2019**, *10*, 1902573.
[41] C. M. Wolff, bandgap_vs_S_vs_for_fixed_CTL.scaps https://zenodo.org/records/10138389/files/bandgap_vs_S_for_fixed_CTL.scaps?download=1 (accessed: November 2023).
[42] M. Burgelman, J. Verschraegen, S. Degrave, P. Nollet, *Prog. Photovoltaics* **2004**, *12*, 143.
[43] M. Burgelman, P. Nollet, S. Degrave, *Thin Solid Films* **2000**, *361-362*, 527.
[44] H. Chen, A. Maxwell, C. Li, S. Teale, B. Chen, T. Zhu, E. Ugur, G. Harrison, L. Grater, J. Wang, Z. Wang, L. Zeng, S. M. Park, L. Chen, P. Serles, R. A. Awni, B. Subedi, X. Zheng, C. Xiao, N. J. Podraza, T. Filleter, C. Liu, Y. Yang, J. M. Luther, S. D. Wolf, M. G. Kanatzidis, Y. Yan, E. H. Sargent, *Nature* **2023**, *613*, 676.
[45] M. A. Faist, T. Kirchartz, W. Gong, R. S. Ashraf, I. McCulloch, J. C. de Mello, N. J. Ekins-Daukes, D. D. C. Bradley, J. Nelson, *J. Am. Chem. Soc.* **2011**, *134*, 685.
[46] F. Steiner, S. Foster, A. Losquin, J. Labram, T. D. Anthopoulos, J. M. Frost, J. Nelson, *Mater. Horiz.* **2015**, *2*, 113.
[47] M. A. Faist, S. Shoaee, S. Tuladhar, G. F. A. Dibb, S. Foster, W. Gong, T. Kirchartz, D. D. C. Bradley, J. R. Durrant, J. Nelson, *Adv. Energy Mater.* **2013**, *3*, 744.
[48] B. Das, I. Aguilera, U. Rau, T. Kirchartz, *Phys. Rev. Mater.* **2020**, *4*, 024602.
[49] C. M. Sutter-Fella, Y. Li, M. Amani, J. W. Ager, F. M. Toma, E. Yablonovitch, I. D. Sharp, A. Javey, *Nano Lett.* **2016**, *16*, 800.
[50] I. L. Braly, D. W. deQuilettes, L. M. Pazos-Outón, S. Burke, M. E. Ziffer, D. S. Ginger, H. W. Hillhouse, *Nat. Photonics* **2018**, *12*, 355.
[51] F. Peña-Camargo, P. Caprioglio, F. Zu, E. Gutierrez-Partida, C. M. Wolff, K. Brinkmann, S. Albrecht, T. Riedl, N. Koch, D. Neher, M. Stolterfoht, *ACS Energy Lett.* **2020**, *5*, 2728.
[52] R. T. Ross, *J. Chem. Phys.* **1967**, *46*, 4590.
[53] U. Rau, *Phys. Rev. B* **2007**, *76*, 8.
[54] J. M. Richter, M. Abdi-Jalebi, A. Sadhanala, M. Tabachnyk, J. P. Rivett, L. M. Pazos-Outón, K. C. Gödel, M. Price, F. Deschler, R. H. Friend, *Nat. Commun.* **2016**, *7*, 1.
[55] K. Suchan, *Ph.D. Thesis*, Lund University, Lund **2023**.
[56] G. F. Samu, C. Janáky, P. V. Kamat, *ACS Energy Lett.* **2017**, *2*, 1860.
[57] K. Datta, B. T. van Gorkom, Z. Chen, M. J. Dyson, T. P. A. van der Pol, S. C. J. Meskers, S. Tao, P. A. Bobbert, M. M. Wienk, R. A. J. Janssen, *ACS Appl. Energy Mater.* **2021**, *4*, 6650.
[58] A. Singareddy, U. K. R. Sadula, P. R. Nair, *J. Appl. Phys.* **2021**, *130*, 225501.
[59] R. A. Kerner, Z. Xu, B. W. Larson, B. P. Rand, *Joule* **2021**, *5*, 2273.
[60] D. O. Tiede, M. E. Calvo, J. F. Galisteo-López, H. Míguez, *J. Phys. Chem. Lett.* **2020**, *11*, 4911.
[61] A. Ruth, M. C. Brennan, S. Draguta, Y. V. Morozov, M. Zhukovskyi, B. Janko, P. Zapol, M. Kuno, *ACS Energy Lett.* **2018**, *3*, 2321.
[62] Q. Jiang, J. Tong, R. A. Scheidt, X. Wang, A. E. Louks, Y. Xian, R. Tirawat, A. F. Palmstrom, M. P. Hautzinger, S. P. Harvey, S. Johnston, L. T. Schelhas, B. W. Larson, E. L. Warren, M. C. Beard, J. J. Berry, Y. Yan, K. Zhu, *Science* **2022**, *378*, 1295.